Activation of Ti–Fe–Cr alloys containing identical AB_2 fractions

Hayoung Kim [a,b], Mohammad Faisal [a,*], Sang-In Lee [a], Jee Yun Jung [a,c], Han-Jin Kim [a,c], Jihyun Hong [a], Young-Su Lee [a,*], Jae-Hyeok Shim [a], Young Whan Cho [a], Do Hyang Kim [b], Jin-Yoo Suh [a]

[a] Center for Energy Materials Research, Korea Institute of Science and Technology, Seoul 02792, Republic of Korea
[b] Department of Materials Science and Engineering, Yonsei University, Seoul 03722, Republic of Korea
[c] Department of Materials Science and Engineering, Korea University, Seoul 02481, Republic of Korea

ABSTRACT

TiFe-based alloys are solid-state hydrogen storage materials operated at room temperature (RT). The current study presents a systematic approach for solving the activation issue (difficulty in the first hydrogenation), one of the major obstacles to the practical application of TiFe alloys, via the use of a secondary AB_2 phase. Based on the Ti–Fe–Cr ternary phase diagram, Ti–Fe–Cr alloys containing 80 at% Ti(Fe,Cr) (AB phase) and 20 at% Ti(Fe,Cr)$_2$ (AB_2 phase) were designed; the Cr concentrations in the AB and AB_2 phase were systematically varied while maintaining fixed phase fractions. Activation at RT was achieved when the overall Cr concentration was higher than 9.7 at%. Analysis of the activation characteristics of the individual phases revealed that the AB_2 phase readily absorbed hydrogen, thereby initiating activation of AB + AB_2 alloys. Notably, higher Cr concentrations enable the AB phase to absorb hydrogen at RT during the activation process, although the kinetics are much slower than that of the co-existing AB_2 phase. The equilibrium hydrogen pressures from the pressure-composition isotherms decrease as the Cr concentration increases, indicating that Cr stabilizes hydrides. Increased hydride stability may also promote the kinetics of the initial hydride formation in both the AB and AB_2 phases. An optimal composition for Ti–Fe–Cr alloys can be designed given the conditions of easy activation at RT and maximum reversible capacity within an operating pressure range.

© 2021 The Author(s). Published by Elsevier B.V.
CC BY-NC-ND 4.0

1. Introduction

Solid-state hydrogen storage is a safe method for hydrogen storage because hydrogen is stored in the form of metal hydrides. TiFe alloys are one of the most promising hydrogen storage alloys because they display a relatively high hydrogen storage capacity (1.9 wt%), forming TiFeH$_{-2}$ [1], under ambient operating pressure conditions and have good reversibility [1,2]. However, activation (the first hydrogenation) is difficult [3] and requires a high temperature (673 K) under a high vacuum condition and a high hydrogen pressure (4.0 MPa) [1]. To improve the activation properties of TiFe-based intermetallics, various approaches have been employed, such as mechanical alloying [4–7], surface modification [8–11], and substitution of other elements. Among these, element substitution is the most convenient and robust solution, and it has been reported that the substitution of a small amount of Cr [12–16], Mn [13,17,18], V

[19], Zr [20], or Ni [21] in TiFe alloys reduces the time required for activation.

In terms of phase equilibrium, there are two primary changes: (i) the formation of a solid solution with TiFe and (ii) the formation of secondary phases. The former has been evidenced by an increase in the lattice parameter of the TiFe phase [14] and the accompanying decrease in the equilibrium pressure of hydrogen absorption and desorption [19,22]. The latter is a characteristic of Ti–Fe phase equilibrium. The Ti–Fe binary system has two intermetallic compounds: TiFe (B2 structure) and TiFe$_2$ (C14 structure, Laves phase). TiFe and TiFe$_2$ belong to the categories of AB and AB_2 compounds, respectively, in which A denotes hydride-forming elements (such as Ti and Zr), and B denotes non-hydride-forming elements (such as Cr, Mn, Fe, and Ni). Because the TiFe phase has a narrow composition range (49.2–52.1 at% Ti) [23], the addition of an alloying element *M* often produces a Ti–Fe–M ternary AB_2 phase.

The presence of AB_2 phases (C14 structure) in TiFe alloys is known to improve the activation and hydrogen absorption kinetics. In studies by Gosselin et al. and Lv et al. [24,25], TiFe alloyed with Zr

or $ZrMn_2$ contained an AB_2 secondary phase in addition to the major AB phase. The fraction of AB_2 increased with the Zr or $ZrMn_2$ content. There was an optimal amount of Zr for activation, and it was concluded that the kinetic enhancement resulted from fast hydrogen diffusion through the secondary phase. Similar studies have been conducted for the TiFe + $ZrCr_2$ system [26]. Lee et al. [16] studied TiFe alloyed with Cr. The addition of Cr to TiFe resulted in $TiCr_2$ as the second phase. As the Cr concentration increases, activation occurs faster. It was envisaged that volume expansion during the hydrogenation of $TiCr_2$ (17.8% according to Johnson [27]) breaks the alloy into smaller pieces, thus exposing fresh surfaces of the TiFe phase, which leads to the easy activation of TiFe [16]. The improved activation is therefore related to the hydrogen absorption properties of the AB_2 phase. For instance, Manickam et al. experimented with AB_2 single-phase alloys with a non-stoichiometry in A site, $(Ti_{0.65}Zr_{0.35})_{1+x}MnCr_{0.8}Fe_{0.2}$ (x = 0, 0.05, 0.075 and 0.1), and confirmed that the alloys were activated at RT without any pretreatment and reached their maximum hydrogen storage capacity within 10 min at 305 K under 1.5 MPa hydrogen pressure [28].

Most studies that emphasized the effect of the AB_2 phase on the activation of TiFe alloys did not characterize the hydrogen storage properties of the AB and AB_2 phases individually, though it is crucial for understanding the role of the AB_2 phase. In addition, in most cases, both the quantity and composition of AB_2 vary simultaneously, making it difficult to identify which property (quantity or composition) is the major contributor to the enhanced activation. In the present study, we explore the hydrogen storage characteristics of Ti–Fe–Cr ternary alloys, which were chosen as a model system to investigate the effect of the AB_2 phase. Cr dissolves in the AB phase and simultaneously forms the AB_2 phase. Based on the Ti–Fe–Cr ternary phase diagram study [29–32], we designed alloys with varying Cr concentrations such that the fraction of the AB_2 phase was constant (80 at% AB and 20 at% AB_2). By fixing the fraction of the AB_2 phase, we excluded the effect of changes in the amount of AB_2 and solely focused on the effect of the composition of the AB_2 and AB phases. Subsequent characterization of AB and AB_2 single-phase alloys with corresponding Cr concentrations was conducted to further elucidate the hydrogen storage properties of the individual phases.

2. Experimental details

2.1. Sample preparation

High-purity Ti (99.995%), Fe (99.9%), and Cr (99.95%) were purchased from RND KOREA. A total of four alloys, labeled A1 to A4 (A*N* alloys, *N* = 1–4), with different Cr concentrations were made. A1 does not contain Cr, and the Cr concentration increases with the sample number. The compositions are summarized in Table 1. Single-phase AB and AB_2 alloys with compositions taken from A3 and A4 (Table 2) were also prepared. The alloys were designated A3-AB, A3-AB_2, A4-AB, and A4-AB_2. The compositions of the eight alloys are marked in the Ti–Fe–Cr ternary phase diagram [32] in Fig. 1.

The alloys were arc melted in an Ar atmosphere, and all samples weighed 30 g (± 0.005 g). Ti was used as a getter (to minimize the absorption of oxygen during melting) and was melted three times before melting the alloys. Ingots were turned over four times to ensure compositional homogeneity. The weight loss of the alloys was less than 1%. The ingots were annealed at 1273 K for a week in vacuum-sealed quartz tubes, and then water quenched immediately after annealing.

2.2. Structural characterization

X-ray diffraction (XRD, Bruker D8 Advance X-ray diffractometer, Cu Kα radiation) was employed for structural analysis. About 1 g of each sample was ball-milled for 5 min at 30 Hz (Retsch mixer mill MM400). The analysis range for the diffraction studies was 20–90° for samples A1–A4. Unlike these alloys, AB and AB_2 single-phase alloys were prepared differently to distinguish the peak more accurately. The analysis range was 20–115°, and the samples were hand-crushed and sieved at 100 μm. Rietveld refinement was performed using the TOPAS software [33].

2.3. Hydrogenation

A custom-designed Sieverts-type apparatus was used to measure the first cycle activation for hydrogen storage. The pressure-composition isotherms (PCI) were obtained using automatically controlled equipment (Particulate Systems HPVA II). For the activation process, a stainless-steel reactor (2 cm^3) was charged with ~300 mg of the samples (ground to a size of 2–3 mm in air). The reactor was evacuated to a rough vacuum of 0.1 Pa for 20 min at 303 K. After evacuation, the samples were exposed to 3.0 MPa H_2 (99.9999% purity) at RT, recording the pressure change to detect the first hydrogenation. Subsequently, to remove residual hydrogen in the samples, the system was heated to 473 K under vacuum. After complete dehydrogenation of the activated samples, the PCI profile was measured. Equilibrium was ensured during the PCI measurements by waiting until the pressure stabilized or the maximum waiting time (150 min) passed before performing each measurement. Samples A1 and A2 did not activate at RT, and an additional treatment, heating at 673 K under vacuum and cooling under 3.0 MPa H_2, was applied.

2.4. Microstructure

The microstructures of the alloys were observed using field-emission scanning electron microscopy (FE-SEM, FEI Inspect F50) in backscattered electron (BSE) mode and electron backscatter diffraction (EBSD) combined with energy dispersive X-ray spectroscopy (EDS) (Bruker Nano e-FlashHR and X-Flash, respectively). The EBSD specimens were mechanically polished and electropolished in a mixed solution of 60% methanol (CH_3OH), 35% butoxyethanol ($C_6H_{14}O_2$), and 5% perchloric acid ($HClO_4$). The EBSD results were processed using orientation imaging microscopy (OIM) analysis software (TexSEM Laboratories, Inc.).

3. Results and discussion

The compositions of the designed alloys A1 to A4 with 20 at% of the AB_2 phase (based on the Ti–Fe–Cr ternary phase diagram at 1273 K from Wang et al. [32]) are listed in Table 1 and marked as triangular symbols in Fig. 1. In Table 1, the measured compositions from SEM-EDS agree with the design compositions within ~1 at%. Fig. 2 shows SEM micrographs of A1 to A4 in BSE mode. It is clearly seen that those alloys are mainly composed of two phases. Based on the relative area and composition, the dark matrix that protrudes forward was identified as the AB phase and the brighter second phase was identified as the AB_2 phase. The compositions of each phase obtained from EDS are listed in Table 2 and marked in the phase diagram in Fig. 1. In Fig. 1, A*N*-AB and A*N*-AB_2 indicate the

Table 1
Design compositions (in at%) of the alloys A1 to A4 and measured compositions using SEM-EDS area analysis.

	Design composition				Measured composition			
	A1	A2	A3	A4	A1	A2	A3	A4
Ti	46.9	47.0	47.4	47.6	46.5	46.5	47.0	47.1
Fe	53.1	45.5	42.7	40.2	53.5	46.2	43.3	41.0
Cr	0	7.5	9.9	12.2	0	7.3	9.7	11.9

Table 2

Compositions (in at%) of the AB and AB$_2$ phases in the alloys A1 to A4 measured using SEM-EDS point analysis.

	A1		A2		A3		A4	
	AB	AB$_2$	AB	AB$_2$	AB	AB$_2$	AB	AB$_2$
Ti	50.0(1)	37.6(7)	50.2(1)	36.9(1)	50.4(2)	37.5(2)	50.4(1)	39.1(2)
Fe	50.0(1)	62.4(7)	46.5(3)	42.3(7)	45.2(2)	35.5(3)	43.7(2)	32.1(2)
Cr	0	0	3.3(3)	20.8(6)	4.4(2)	27.0(5)	5.9(2)	28.8(4)
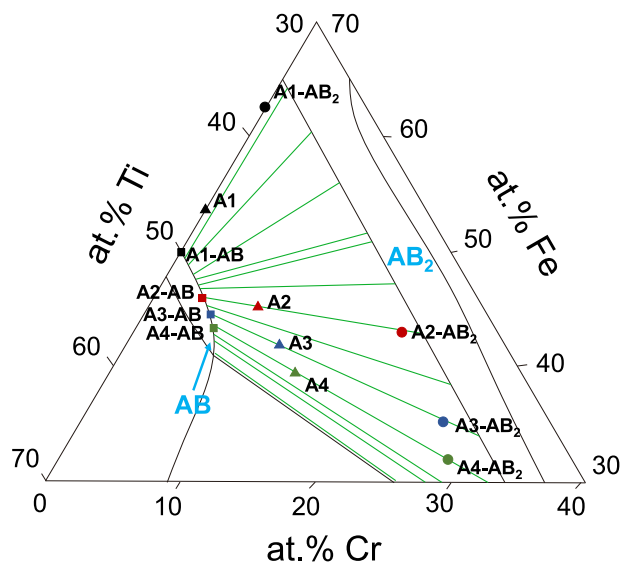
Fig. 1. Compositions of the alloys A1 to A4 on the Ti–Fe–Cr partial ternary phase diagram at 1273 K. AN-AB and AN-AB$_2$ indicate the compositions of the AB and AB$_2$ phases, respectively, in the AN alloy (N = 1–4).

compositions of the AB and AB$_2$ phases, respectively, in the AN alloys.

As expected, the compositions of the phases AN-AB fall on the phase boundary of the AB single-phase region in the ternary phase diagram. The compositions AN-AB$_2$ in Fig. 1, however, are slightly shifted toward a Ti-rich composition and fall in the AB-AB$_2$ two-phase region. The composition analysis indicates that our alloys may

not have reached full thermodynamic equilibrium due to the different sample preparation conditions such as annealing [31].
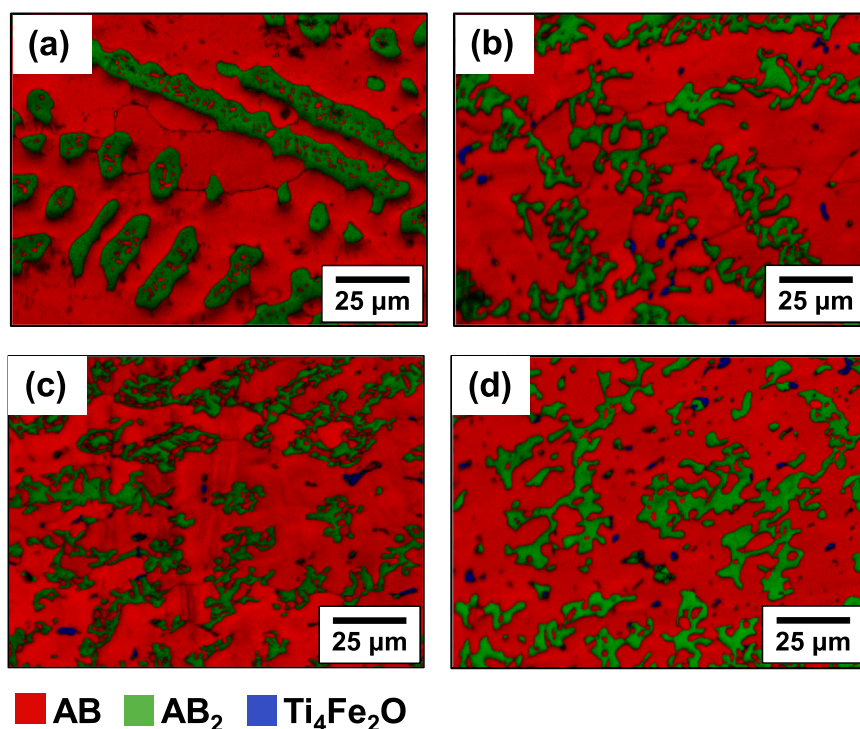
EBSD phase maps are overlapped with image quality (IQ) maps of the samples in Fig. 3. Along with the AB and AB$_2$ phases, a small amount of Ti$_4$Fe$_2$O (space group *Fd-3m*) [34] was found. These three phases are consistently found in the XRD patterns of the samples presented in Fig. 4. The phase fractions obtained from the EBSD area analysis and Rietveld refinement of the XRD data are compared in Table 3. The Rietveld refinement results for each alloy are shown in Figs. S1–S4. The proportions of the AB and AB$_2$ phases agree very well between the two results, and approximately 20% of the AB$_2$ phase was present regardless of the alloy composition. The proportion of the AB$_2$ phase was slightly larger (especially in A4) due to the deviation of the AB$_2$ phase composition toward a Ti-rich composition, as shown in Fig. 1. We note that the relative uncertainty of the amount of Ti$_4$Fe$_2$O is rather large. In the XRD analysis, the peak intensities are very small except for the most intense peak, and in EBSD analysis, the imaged area is insufficient to represent the overall phase amount.

The lattice parameters of the AB and AB$_2$ phases calculated from the Rietveld refinement results are listed in Table S1. The lattice parameter increased as the Cr concentration increased for both the AB and AB$_2$ phases. As shown in Table 2, the atomic concentration of Ti remained almost unchanged regardless of the Cr concentration in both the AB and AB$_2$ phases, which suggests that Cr mainly replaces Fe. Therefore, the composition of the AB and AB$_2$ phases can be expressed as Ti(Fe,Cr) and Ti(Fe,Cr)$_2$. Because the atomic radius of Cr is larger than that of Fe, a higher Cr concentration led to a larger lattice parameter, in agreement with Zadorozhnyy et al. [14].

The combined EBSD and XRD results confirm that the alloys were synthesized as originally designed. We then investigated how the Cr concentration in the AB and AB$_2$ phases affects the activation (first
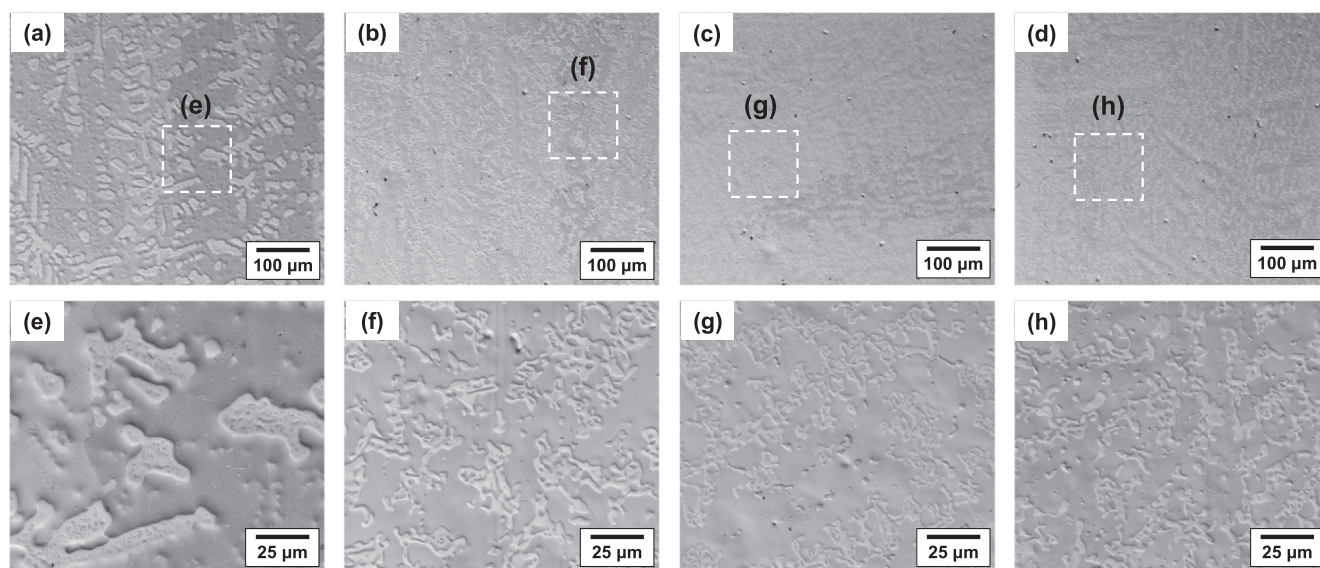
Fig. 2. BSE micrographs of (a) A1, (b) A2, (c) A3, and (d) A4 at 500× magnification and (e) A1, (f) A2, (g) A3, and (h) A4 at 2000× magnification.

AB **AB$_2$** **Ti$_4$Fe$_2$O**

Fig. 3. EBSD phase identification overlapped with image quality (IQ) maps of the alloys: (a) A1, (b) A2, (c) A3, and (d) A4. The AB, AB$_2$, and Ti$_4$Fe$_2$O phases are colored red, green, and blue, respectively. (For interpretation of the references to color in this figure legend, the reader is referred to the web version of this article.)

hydrogenation) characteristics of these alloys. Fig. 5 shows the activation for the A1 to A4 samples measured at RT under 3.0 MPa H$_2$. Activation occurred more easily as the Cr concentration increased. Samples with no Cr (A1) and a small amount of Cr (A2) did not activate at RT. These two samples were activated by heating at 673 K under a vacuum and cooling under 3.0 MPa H$_2$. To better understand how Cr promotes activation, experiments were conducted for the individual AB and AB$_2$ phases of A3 and A4. The compositions are shown in Table 2 and Fig. 1, and the alloys were prepared following the same procedure that was used for A1–A4.

The XRD data and the corresponding Rietveld refinement result of four single-phase alloys (A3-AB, A3-AB$_2$, A4-AB, and A4-AB$_2$) in Figs. S5-S8 show that they are mainly composed of a single phase. Phase fractions obtained from Rietveld refinement of the XRD data are listed in Table 4. The phase analysis results show that the main phase accounts for more than 90% and the proportion of the minor phases is very small. The small amount of AB phase found in (A3, A4)-AB$_2$ indicates that the starting compositions marked in Fig. 1 indeed belong to the two-phase region as discussed above. Importantly, the diffraction peaks of AB$_2$ are not observed in the XRD data of the AB single-phase alloy. BSE micrographs in Fig. S9 also support that those four alloys are almost a single phase.

The time evolution of the amount of absorbed hydrogen during activation of these four alloys is shown in Fig. 6. Consistent with the activation results of the two-phase alloys in Fig. 5, the kinetics of the first hydrogenation became faster as the Cr concentration increased for both the AB and AB$_2$ phases. Notably, the AB$_2$ alloys readily absorbed hydrogen without an incubation time. What is rather surprising is that, against the generally accepted idea that the AB single phase is difficult to activate at RT, even A3-AB and A4-AB absorbed hydrogen after a few hours of incubation time. This remarkable result reveals that although AB$_2$ plays a major role in accelerating activation, the AB single phase, here Ti(Fe,Cr), can be activated at RT when the Cr concentration is above a critical value, which would lie between 3.3 at% (Cr concentration of AB in A2) and 4.4 at% (Cr concentration of A3-AB). It has not yet been reported that an

experimentally confirmed single-phase Ti(Fe,Cr) alloys can be activated at RT. In a previous study on Ti–Fe–Cr ternary alloys, Lee et al. showed that the alloy, in which AB and AB$_2$ phases coexisted, was activated at RT, but emphasized that this was due to the presence of the AB$_2$ phase [16].

To understand the hydrogen storage characteristics of these alloys, the PCI profiles of all the alloys were measured at RT and are plotted in Fig. 7. Hydrogen absorption proceeds in two steps [1], sequentially forming Ti(Fe,Cr)H and Ti(Fe,Cr)H$_2$ as the hydrogen partial pressure increases; the corresponding two plateaus are shown in Fig. 7a. Within the applied pressure range, the hydrogen capacity of AB (1.78 wt% for A4-AB and 1.69 wt% for A3-AB) is much larger than that of AB$_2$ (0.65 wt% for A4-AB$_2$ and 0.37 wt% for A3-AB$_2$), as presented in Fig. 7b. The equilibrium hydrogen pressure of TiCr$_2$ (AB$_2$) at RT is quite high [27], and that of Ti(Fe,Cr)$_2$ would be even higher because TiFe$_2$ hardly absorbs hydrogen [1]. Therefore, Ti(Fe,Cr)$_2$ does not form hydrides but instead forms a solid solution with hydrogen, which is why the plateau of the AB$_2$ phase is not observed and the amount of absorbed hydrogen is limited. In this sense, although the AB$_2$ phase promotes activation, the amount should be minimized to avoid significantly reducing the overall hydrogen storage capacity. As expected from the results in Fig. 5, Fig. 7a again confirms that a higher Cr concentration increases the maximum hydrogen storage capacity (from 1.32 wt% of A1 to 1.63 wt% of A4), and it is evident that Cr replacement lowers the equilibrium hydrogen pressure for both the AB and AB$_2$ phases, yielding more stable hydrides and solid solutions, respectively.

The systematic change in the desorption pressure and the lattice parameter of the AB phase as a function of Cr concentration is illustrated in Fig. 8. Here, we compare desorption pressure instead of absorption pressure because the desorption pressure tends to be closer to the real equilibrium pressure while the absorption pressure is more susceptible to hysteresis effect [35]. The desorption pressures were taken at 0.6 wt% H$_2$ from the desorption curves in Fig. 7a. Although Fig. 7a illustrates the PCI profiles of the two-phase alloys, the first plateau region is mainly associated with AB phase. The
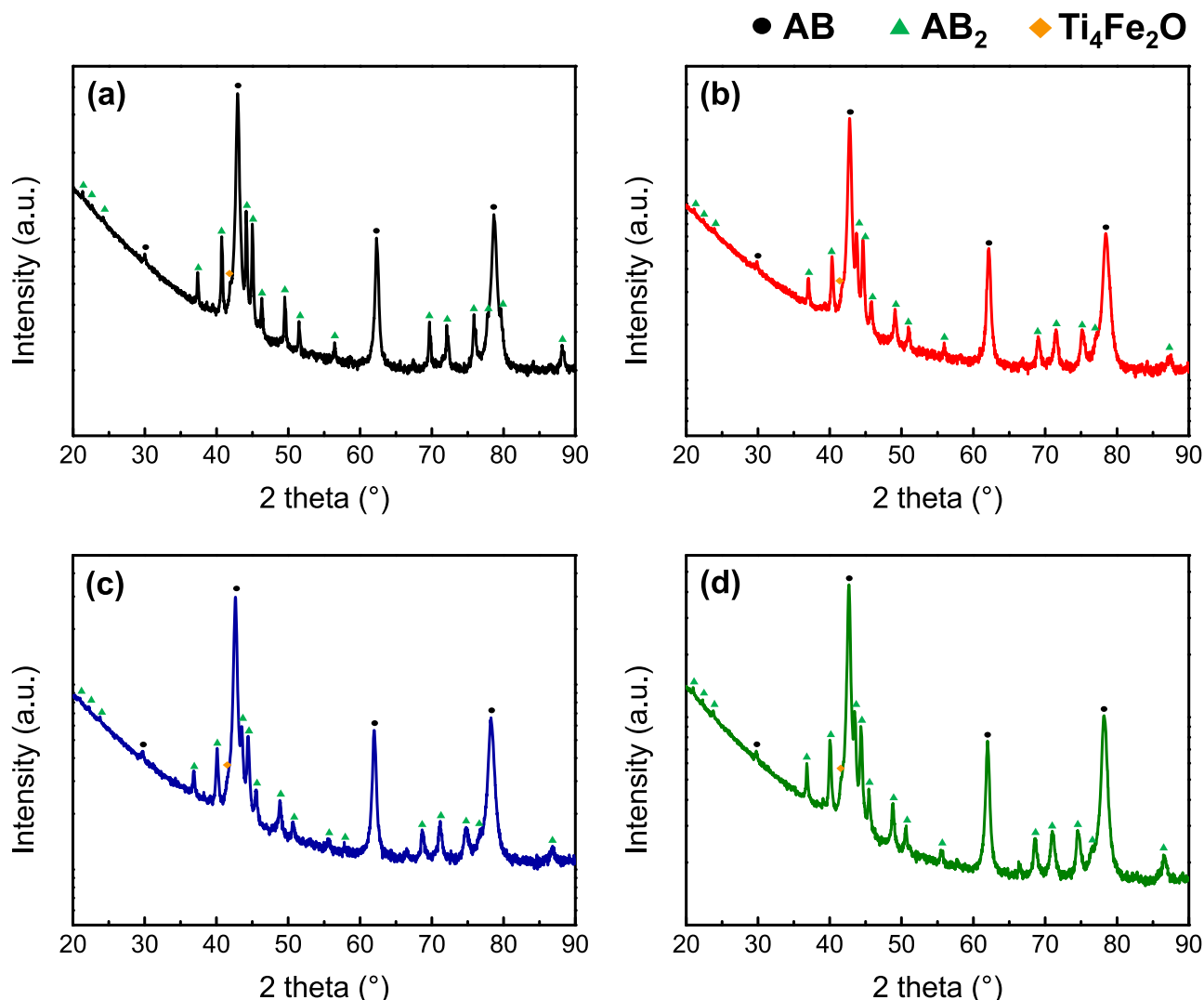
● **AB**   ▲ **AB$_2$**   ◆ **Ti$_4$Fe$_2$O**

Fig. 4. XRD patterns of the four alloys: (a) A1, (b) A2, (c) A3, and (d) A4. The intensity is presented in the logarithmic scale for better visibility of small peaks. The AB, AB$_2$, and Ti$_4$Fe$_2$O phases are found in all the alloys.

Table 3
Phase fractions of the A1 to A4 alloys obtained from the EBSD micrographs (area%) and the XRD data (at%).

	EBSD			XRD		
	AB	AB$_2$	Ti$_4$Fe$_2$O	AB	AB$_2$	Ti$_4$Fe$_2$O
A1	79.7(2)	20.3(3)	0	77.0(2)	20.6(1)	2.4(2)
A2	77.4(2)	21.5(3)	1.1(4)	74.5(3)	21.8(2)	3.7(2)
A3	78.3(2)	21.1(3)	0.6(5)	74.4(3)	22.9(2)	2.7(2)
A4	74.9(2)	24.4(4)	0.7(4)	72.7(2)	23.7(2)	3.6(2)

desorption pressure taken at 0.6 wt% H$_2$ for A3-AB and A4-AB in Fig. 7b are 0.07 and 0.04 MPa, respectively, which are very similar to 0.09 and 0.05 MPa for A3 and A4, respectively. The lattice parameter and the logarithmic value of the pressure vary almost linearly with the Cr concentration, exhibiting the opposite trend. Such information can be used to design TiFe alloys with target equilibrium pressures [13,36].

The interplay between thermodynamics and kinetics upon Cr substitution can be viewed in several aspects. In the AB single-phase alloy, the cell volume increases as Cr replaces Fe site. As more Cr replaces Fe, the equilibrium pressure decreases as in Fig. 8, meaning that the hydride becomes more stable. First, such thermodynamic change appears to be correlated with the hydrogen absorption
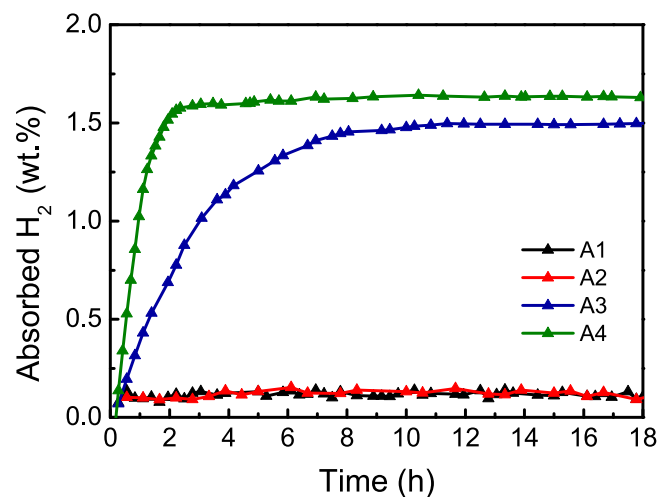
Fig. 5. First hydrogenation at 303 K under 3.0 MPa H$_2$ for the four AN alloys. A1, A2, A3, and A4 are shown in black, red, navy, and olive, respectively. (For interpretation of the references to colour in this figure legend, the reader is referred to the web version of this article.)

Table 4
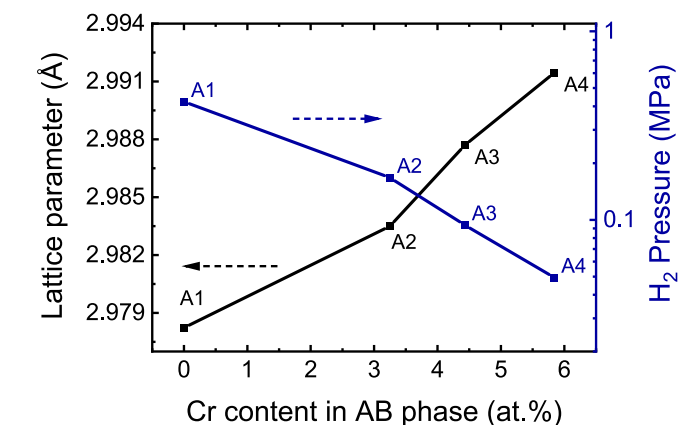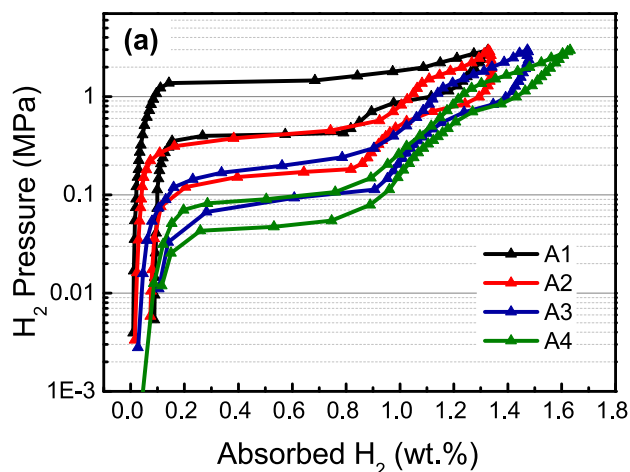Phase fractions of (A3, A4)-(AB, AB$_2$) alloys obtained from the XRD data (at%).

	AB	AB$_2$	Ti$_4$Fe$_2$O
A3-AB	96.6(3)	0	3.4(3)
A3-AB$_2$	2.3(1)	94.4(3)	3.3(3)
A4-AB	97.5(3)	0	2.5(3)
A4-AB$_2$	5.6(1)	91.2(2)	3.2(2)
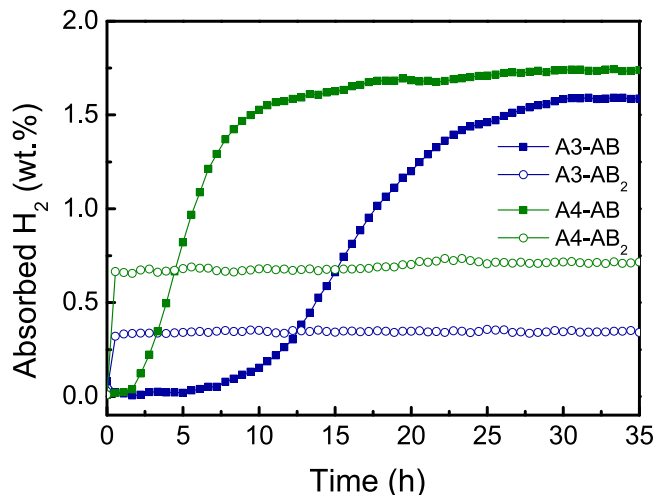
Fig. 6. First hydrogenation at 303 K under 3.0 MPa H$_2$ for the (A3, A4)-(AB, AB$_2$) alloys. A3 and A4 are colored navy and olive, respectively.

Fig. 8. Lattice parameter of the AB phase and desorption pressure as a function of Cr concentration in the AB phase.

kinetics in Fig. 6: the increased thermodynamic driving force toward the more stable hydride may as well expedite initial hydrogen absorption. Second, the absorbed amount of hydrogen under a given hydrogen pressure increases with Cr concentration as shown in Figs. 6 and 7 due to more favorable hydride formation. The increased hydrogen absorption would then lead to a larger volume expansion that would pulverize the alloy, which in turn can accelerate subsequent hydrogen absorption by exposing larger surface area. The mechanism behind the RT activation of Ti(Fe,Cr) is worth further attention.

Summarizing the result thus far, the optimal Cr concentration for achieving activation at RT lies somewhere between that in A2 and that in A3, as discussed previously. Fortuitously, this amount of Cr replacement yields an AB phase with ~4 at% Cr, which desorbs hydrogen under ambient pressure (~0.1 MPa) at RT (see Fig. 8). Several previous studies have discussed the improved activation

characteristics of Ti–Fe–Cr alloys [14,16] and some evidence is provided on the formation of the AB$_2$ phase. However, its composition and phase amount were not identified; therefore, the role of AB$_2$ in Ti–Fe–Cr alloys remains elusive. This study clearly demonstrates that there is a critical concentration of Cr in Ti(Fe,Cr)$_2$, between 20.8 and 27.0 at%, that allows activation at RT. One interesting feature of the Ti–Fe–Cr phase diagram in Fig. 1 is that in the AB-AB$_2$ two-phase region, the Cr concentration in the AB$_2$ phase changes to a larger degree than that in the AB phase with a change in the overall Cr concentration. Therefore, without significantly affecting the hydrogen storage capacity of the AB phase, the composition of the AB$_2$ phase can be adjusted such that activation at RT is feasible. The next task is to optimize the amount of the AB$_2$ phase. In Fig. 7a, if we operate a Ti–Fe–Cr alloy with a composition between A2 and A3 in the pressure range of 0.1 MPa (for desorption) to 3.0 MPa (for absorption), the reversible hydrogen storage capacity would be ~1 wt%. This can be increased by reducing the amount of the AB$_2$ phase, with the condition that activation at RT is achieved within a practical time limit.

We find an additional benefit of Cr replacement: the hysteresis decreases from sample A1 to A4 in Fig. 7a. To visualize the degree of hysteresis, d(absorbed H$_2$)/$d$log(H$_2$ pressure) (denoted as d(H$_2$ in wt%)/$d$log$P$) is calculated and shown in Fig. 9. This derivative should display a peak in the plateau region, and two peaks, corresponding to the first and second plateaus, are observed in Fig. 9. The peak from the second plateau is small, making it difficult to distinguish. Here, we focus on the peak shift from desorption to
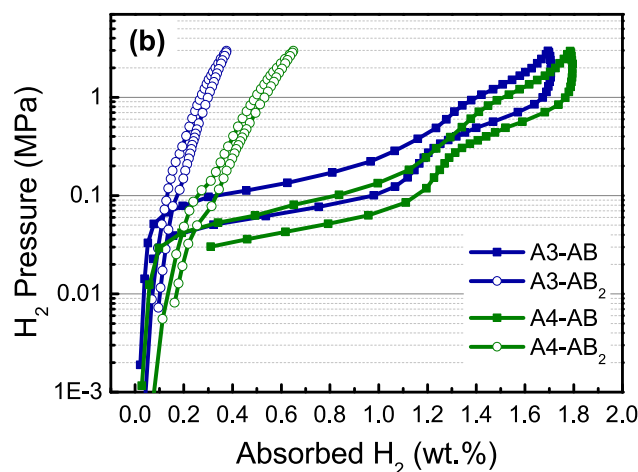
Fig. 7. PCI curves at 303 K for the eight Ti–Fe–Cr alloys: (a) A1 to A4 (two-phase alloys) and (b) (A3, A4)-(AB, AB$_2$) (single-phase alloys).
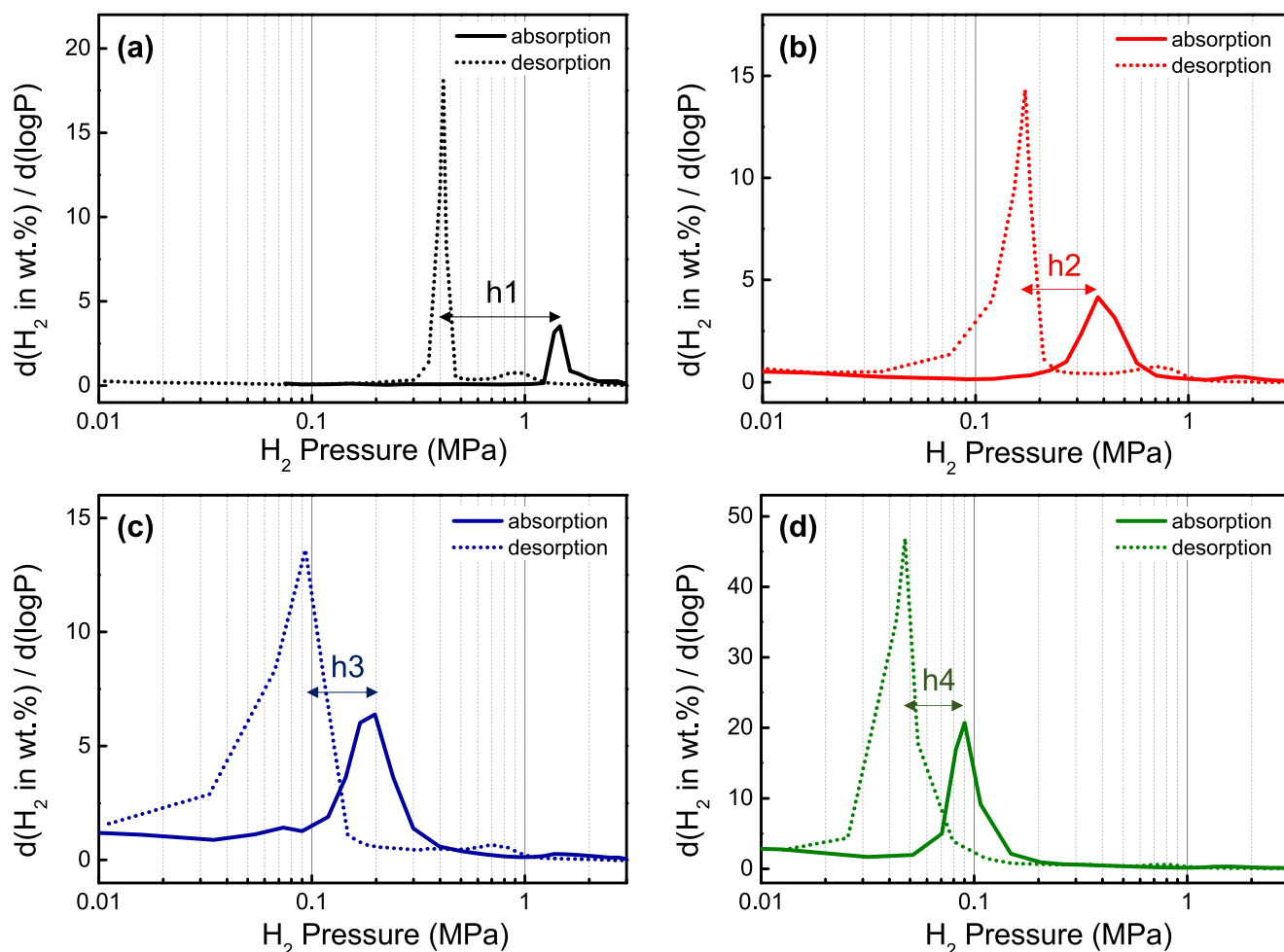
Fig. 9. Derivatives of the absorbed H$_2$ (wt%) with respect to H$_2$ pressure (MPa) (denoted as d(H$_2$ in wt%)/$d$log$P$): (a) A1, (b) A2, (c) A3, and (d) A4.

absorption, which is for the first plateau (denoted as h1 to h4). The logarithmic pressure difference (i.e., hysteresis) decreases (h1 > h2 > h3 > h4) with increasing Cr concentration. The study conducted by Reilly [37] reveals that TiMn$_2$ shows a high hysteresis of 20 MPa while TiCr$_2$ shows negligible hysteresis. This suggests that a larger atomic size of Cr leads to a larger unit cell volume and thus results in a larger interstitial hole size [38,39], which reduces lattice strain during hydrogen absorption that is manifested as lowered pressures for hydrogen absorption and hysteresis [40]. Similarly, the lesser degree of hysteresis revealed here may as well be another reason why the first hydrogenation of Cr-substituted alloys is more facile than that of those without Cr [12]. The increased lattice parameter may reduce the strain during hydrogenation, thereby lowering the barrier caused by hysteresis and rendering the phase transition easier.

4. Conclusions

The activation characteristics of the Ti–Fe–Cr ternary alloy system, with 20 at% AB$_2$, was systematically investigated. While A1 and A2, with no or a small amount of Cr, could not be activated at RT, A3 and A4, with higher amounts of Cr, were activated at RT. The minimum amount of Cr required for activation at RT therefore lies between 7.3 at% (A2) and 9.7 at% (A3). Characterization of the AB and AB$_2$ single phases revealed that the easy activation mainly relies on the prompt hydrogen absorption of the AB$_2$ phase, and the Cr concentration in the AB$_2$ phase is critical. In addition, the increased Cr concentration facilitates hydrogen absorption even in the AB single-

phase alloys, which has not been reported previously. The AB$_2$ phase promotes the initial activation of the AB phase, but AB can also be activated by itself when it contains a sufficient amount of Cr. The improved absorption kinetics may partly originate from the increasing hydride stability with increasing Cr concentration, as shown in the PCI data.

The optimal composition of the Ti–Fe–Cr alloy, which allows easy activation at RT and reversible hydrogen storage near ambient pressure, can be found between the composition of A2 and A3. The hydrogen storage capacity can be further improved by minimizing the amount of the AB$_2$ phase while maintaining the composition of the AB and AB$_2$ phases, i.e., moving along the tie line of the AB-AB$_2$ two-phase equilibrium region. Such a strategy can be employed to design other TiFe ternary or quaternary alloys that utilize the AB$_2$ phase to achieve activation at RT.

CRediT authorship contribution statement

Declaration of Competing Interest

The authors declare that they have no known competing financial interests or personal relationships that could have appeared to influence the work reported in this paper.

Acknowledgments

Appendix A. Supporting information

Supplementary data associated with this article can be found in the online version at doi:10.1016/j.jallcom.2021.158876.

References

[1] J.J. Reilly, R.H. Wiswall, Formation and properties of iron titanium hydride, Inorg. Chem. 13 (1974) 218–222.

[2] T. Schober, D.G. Westlake, The activation of FeTi for hydrogen storage: a different view, Scr. Metall. 15 (1981) 913–918.

[3] T. Schober, On the Activation of Feti for Hydrogen Storage, J. Less Common Met. 89 (1983) 63–70.

[4] P. Lv, M.N. Guzik, S. Sartori, J. Huot, Effect of ball milling and cryomilling on the microstructure and first hydrogenation properties of TiFe+4 wt% Zr alloy, J. Mater. Res. Technol. 8 (2019) 1828–1834.

[5] G. Romero, P. Lv, J. Huot, Effect of ball milling on the first hydrogenation of TiFe alloy doped with 4 wt% (Zr + 2Mn) additive, J. Mater. Sci. 53 (2018) 13751–13757.

[6] C.H. Chiang, Z.H. Chin, T.P. Perng, Hydrogenation of TiFe by high-energy ball milling, J. Alloys Compd. 307 (2000) 259–265.

[7] T. Haraki, K. Oishi, H. Uchida, Y. Miyamoto, M. Abe, T. Kokaji, S. Uchida, Properties of hydrogen absorption by nano-structured FeTi alloys, Int. J. Mater. Res. 99 (2008) 507–512.

[8] X.Y. Liu, P.K. Chu, C.X. Ding, Surface modification of titanium, titanium alloys, and related materials for biomedical applications, Mater. Sci. Eng. R. Rep. 47 (2004) 49–121.

[9] M. Williams, M.V. Lototsky, M.W. Davids, V. Linkov, V.A. Yartys, J.K. Solberg, Chemical surface modification for the improvement of the hydrogenation kinetics and poisoning resistance of TiFe, J. Alloys Compd. 509 (2011) S770–S774.

[10] M.W. Davids, M. Lototskyy, A. Nechaev, Q. Naidoo, M. Williams, Y. Klochko, Surface modification of TiFe hydrogen storage alloy by metal-organic chemical vapour deposition of palladium, Int. J. Hydrog. Energy 36 (2011) 9743–9750.

[11] G. Sicking, B. Jungblut, Surface TiHn as the catalytically active species for the hydrogen absorption by TiFe; a SX-APS investigation supplemented by AES, Surf. Sci. 127 (1983) 255–270.

[12] T. Yang, P. Wang, C.Q. Xia, N. Liu, C.Y. Liang, F.X. Yin, Q. Li, Effect of chromium, manganese and yttrium on microstructure and hydrogen storage properties of TiFe-based alloy, Int. J. Hydrog. Energy 45 (2020) 12071–12081.

[13] M.H. Mintz, S. Vaknin, S. Biderman, Z. Hadari, Hydrides of ternary TiFexM1−x (M = Cr, Mn, Co, Ni) intermetallics, J. Appl. Phys. 52 (1981) 463–467.

[14] V.Y. Zadorozhnyy, S.N. Klyamkin, M.Y. Zadorozhnyy, O.V. Bermesheva, S.D. Kaloshkin, Mechanical alloying of nanocrystalline intermetallic compound TiFe doped by aluminum and chromium, J. Alloys Compd. 586 (2014) S56–S60.

[15] S.M. Lee, T.P. Perng, H.K. Juang, S.Y. Chen, W.Y. Chen, S.E. Hsu, Microstructures and hydrogenation properties of TiFe1−xMx alloys, J. Alloys Compd. 187 (1992) 49–57.

[16] S. Lee, T. Perng, Effect of the second phase on the initiation of hydrogenation of TiFe1−xMx (M = Cr, Mn) alloys, Int. J. Hydrog. Energy 19 (1994) 259–263.

[17] D. Dew-Hughes, The addition of Mn and Al to the hydriding compound FeTi: Range of homogeneity and lattice parameters, Metall. Trans. A 11 (1980) 1219–1225.

[18] N. Nishimiya, T. Wada, A. Matsumoto, K. Tsutsumi, Hydriding characteristics of zirconium-substituted FeTi, J. Alloys Compd. 313 (2000) 53–58.

[19] H. Miyamura, T. Sakai, N. Kuriyama, H. Tanaka, I. Uehara, H. Ishikawa, Hydrogenation and phase structure of Ti–Fe–V alloys, J. Alloys Compd. 253 (1997) 232–234.

[20] C. Gosselin, J. Huot, Hydrogenation properties of TiFe doped with zirconium, Materials 8 (2015) 7864–7872.

[21] S.M. Lee, T.P. Perng, Correlation of substitutional solid solution with hydrogenation properties of TiFe1−xMx (M = Ni, Co, Al) alloys, J. Alloys Compd. 291 (1999) 254–261.

[22] Z. Chen, X. Xiao, L. Chen, X. Fan, L. Liu, S. Li, H. Ge, Q. Wang, Development of Ti–Cr–Mn–Fe based alloys with high hydrogen desorption pressures for hybrid hydrogen storage vessel application, Int. J. Hydrog. Energy 38 (2013) 12803–12810.

[23] H. Bo, J. Wang, L. Duarte, C. Leinenbach, L.-B. Liu, H.-S. Liu, Z.-P. Jin, Thermodynamic re-assessment of Fe–Ti binary system, Trans. Nonferrous Met. Soc. China 22 (2012) 2204–2211.

[24] C. Gosselin, D. Santos, J. Huot, First hydrogenation enhancement in TiFe alloys for hydrogen storage, J. Phys. D Appl. Phys. 50 (2017) 375303.

[25] P. Lv, Z. Liu, V. Dixit, Improved hydrogen storage properties of TiFe alloy by doping (Zr+2V) additive and using mechanical deformation, Int. J. Hydrog. Energy 44 (2019) 27843–27852.

[26] T. Ha, S.-I. Lee, J. Hong, Y.-S. Lee, D.-I. Kim, J.-Y. Suh, Y.W. Cho, B. Hwang, J. Lee, J.-H. Shim, Hydrogen storage behavior and microstructural feature of a TiFe–ZrCr2 alloy, J. Alloys Compd. 853 (2021) 157099.

[27] J.R. Johnson, Reaction of hydrogen with the high temperature (C14) form of TiCr2, J. Less Common Met. 73 (1980) 345–354.

[28] K. Manickam, D.M. Grant, G.S. Walker, Optimization of AB2 type alloy composition with superior hydrogen storage properties for stationary applications, Int. J. Hydrog. Energy 40 (2015) 16288–16296.

[29] I.I. Kornilov, N.G. Boriskina, The TiCr2–TiFe2 system, Russ. J. Inorg. Chem. 9 (1964) 388–390.

[30] N.G. Boriskina, I.I. Kornilov, A ternary metallic compound formed in the iron–chromium–titanium system, Russ. J. Inorg. Chem. 4 (1959) 986–987.

[31] N.G. Boriskina, I.I. Kornilov, Equilibrium diagram of the chromium–iron–titanium system, Russ, J. Inorg. Chem. 9 (1964) 636–639.

[32] S. Wang, K. Wang, G.Y. Chen, L. Zhu, Z.W. Qin, X.G. Lu, C.H. Li, Thermodynamic modeling of Ti–Fe–Cr ternary system, Calphad 56 (2017) 160–168.

[33] TOPAS version 5, Bruker AXS GmbH, Karlsruhe, Germany.

[34] B. Rupp, On the change in physical properties of Ti4−xFe2+xOy during hydrogenation I: Activation behaviour of ternary oxides Ti4−xFe2+xOy and β-Ti, J. Less Common Met. 104 (1984) 51–63.

[35] M.V. Lototskyy, New model of phase equilibria in metal - hydrogen systems: Features and software, Int. J. Hydrog. Energy 41 (2016) 2739–2761.

[36] J.Y. Jung, Y.-S. Lee, J.-Y. Suh, J.-Y. Huh, Y.W. Cho, Tailoring the equilibrium hydrogen pressure of TiFe via vanadium substitution, J. Alloys Compd. 854 (2021) 157263.

[37] J.J. Reilly, Applications of Metal Hydrides, in: A.F. Andresen, A.J. Maeland (Eds.), Hydrides for Energy Storage, Pergamon, 1978, pp. 527–550.

[38] C.E. Lundin, F.E. Lynch, C.B. Magee, A correlation between the interstitial hole sizes in intermetallic compounds and the thermodynamic properties of the hydrides formed from those compounds, J. Less Common Met. 56 (1977) 19–37.

[39] B.H. Liu, D.M. Kim, K.Y. Lee, J.Y. Lee, Hydrogen storage properties of TiMn2-based alloys, J. Alloys Compd. 240 (1996) 214–218.

[40] A. Guéguen, M. Latroche, Influence of the addition of vanadium on the hydrogenation properties of the compounds TiFe0.9Vx and TiFe0.8Mn0.1Vx (x = 0, 0.05 and 0.1), J. Alloys Compd. 509 (2011) 5562–5566.